ACS APPLIED NANO MATERIALS

www.acsanm.org Article

Boron-Doped Biomass Carbon Nanostructures as Electrocatalysts for the Two-Electron Oxygen Reduction Reaction

Xiang Xu, Ruting Xu, Yuying Zhao, Yuhan Wu, Qixin Yuan, Kang Sun, Shengchun Hu,* Jianchun Jiang, and Mengmeng Fan*

Cite This: *ACS Appl. Nano Mater.* 2024, 7, 18912−18919 Read Online

ACCESS | Metrics & More | Article Recommendations | Supporting Information

ABSTRACT: Highly active B atom dopants were successfully introduced into a biomass carbon matrix as promising electrocatalysts for the two-electron oxygen reduction reaction (2e$^-$ ORR) to synthesize hydrogen peroxide (H_2O_2) by decomposing boron nanosheets with flash Joule heating (FJH) progress. Moreover, the FJH process can greatly improve the graphitization of biomass carbon leading to rapid electron transfer during electrocatalysis. The as-prepared B atom−doped carbon nanomaterial (f-B_s-C) showed greatly enhanced 2e$^-$ ORR performance with outstanding H_2O_2 selectivity (91−94%) at 0.25−0.6 V vs reversible hydrogen electrode (RHE) measured via a rotating ring-disk electrode (RRDE) in an alkaline electrolyte, and the Faradaic efficiency was still greater than 80% during 11 h with a mass activity of 798 mmol $g_{catalyst}^{-1}$ h^{-1} in an actual three-electrode flow cell setup. The overall catalytic performance is preferable to the majority of reported carbon-based catalysts. Density functional theory showed that the O atom connected with B atoms can induce charge density deficiency on the B site acting as high catalytic sites. This research provides an exploration to fabricate heteroatom dopants to enhance the catalytic capability of biomass-based carbon catalysts.

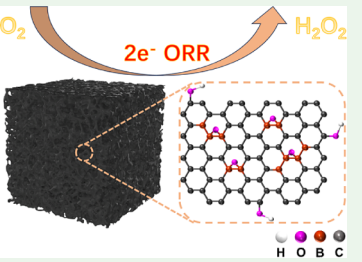

KEYWORDS: *two-electron oxygen reduction reaction, B atom dopant, biomass carbon, flash Joule heating, electrocatalyst*

1. INTRODUCTION

Hydrogen peroxide (H_2O_2) is an environmentally friendly oxidizing agent extensively used in pulp and paper, chemical synthesis, wastewater treatment, and other industrial fields.[1−3] Currently, the main producing process of H_2O_2 is the traditional anthraquinone oxidation process, which has the drawbacks of generating much pollution, consuming high energy, and security risk of transportation.[4,5] The synthesis method of H_2O_2 by electrochemical two-electron oxygen reduction reaction (2e$^-$ ORR) has been suggested by researchers as a substitute for the anthraquinone oxidation process in future industrial production, which can be due to the benefits of a sustainable and safe synthesis process.[6,7] However, the 2e$^-$ ORR synthesis process and the four-electron ORR, which produces H_2O, usually occur simultaneously.[8,9] Consequently, the design of preparative methods with highly active and selective catalysts is crucial to realize the H_2O_2 synthesis via the 2e$^-$ ORR process.[10]

Carbon nanomaterials are promising substitutes for metal catalysts in the field of electrocatalysis due to the advantages of diverse nanostructures, excellent conductivity, and tunable electrochemical properties.[11,12] Especially for biomass carbon nanomaterials, their raw material supply is sufficient at a low price.[13] However, compared to metal-based electrocatalysts such as single metal atoms or cluster catalysts, there is still an inferior 2e$^-$ ORR catalytic capability for metal-free carbon catalysts.[14] To enhance the overall electrocatalytic performance, single or multiple catalytic active sites are introduced into porous biomass carbon materials through defect engineering and heteroatom doping methods.[15,16] In particular, heteroatom doping can introduce richer catalytic active sites to carbon nanomaterials.[17] Among them, common nonmetallic doping heteroatoms include O, B, N, S, P, etc. For one typical example, O-doped or O,N-codoped carbon nanomaterials showed good 2e$^-$ ORR performance with H_2O_2 selectivity of over 90%.[18,19] In addition, it has been shown that B atoms can be readily doped into a carbon skeleton, thereby selectively promoting the ORR.[20,21] According to density functional theory (DFT) simulations, the B atom as the active site has almost zero overpotential for the formation of *OOH intermediates in the 2e$^-$ ORR.[22] Therefore, the B atom is the most efficient active site acting in the 2e$^-$ ORR compared to other heteroatoms.[23]

Carbon nanomaterials prepared from B atom−doped carbon black, reduced graphene oxide, and other carbon substrates have been reported to significantly improve the catalytic performance of the 2e$^-$ ORR, but there are still many problems such as low catalytic selectivity and poor stability.[22,23] Recently, the flash Joule heating (FJH) method has been

Received: May 9, 2024
Revised: July 23, 2024
Accepted: July 28, 2024
Published: August 6, 2024

https://doi.org/10.1021/acsanm.4c02704
ACS Appl. Nano Mater. 2024, 7, 18912−18919

widely used as a rapid pyrolysis strategy for tuning the overall catalyst structure. For example, Tian et al. synthesized ultrasmall nanoparticles derived from metal−organic skeletons by the FJH method, and the prepared catalysts exhibited high catalytic activity and stability in the N_2 reduction reaction.[24] In addition, the FJH method has been used to achieve the conversion of nongraphitized carbon materials to highly crystalline nanoscale graphitized carbon and has resulted in a reduction in the overall defect density of the carbon material.[25,26] Compared with the conventional calcination method, the simple treatment process of the FJH method can shorten the synthesis time and modulate the chemical reaction state of the active sites, which greatly improves the catalytic capability.[27] However, the structure−activity relationship between highly graphitized B-doped biomass carbon nanomaterials by Joule heating used for the $2e^-$ ORR has not yet been reported.

In this research, we fabricated a B atom−doped biomass carbon nanomaterial (f-B_s-C) via an FJH treatment process with exfoliated boron nanosheets (BNs) as the B dopant. Compared to the general pyrolysis process with a tube furnace, Joule heating with flash pyrolysis in a few seconds can avoid the total decomposition of BNs, which can guarantee the smooth doping of B atoms into the biomass carbon matrix. Therefore, the f-B_s-C showed high catalytic performance to $2e^-$ ORR with the H_2O_2 selectivity (91−94%) at 0.25−0.6 V versus reversible hydrogen electrode (RHE). After a 11 h measurement in a three-electrode flow cell setup, the Faradaic efficiency remained over 80% with a high mass activity of 798 mmol $g_{catalyst}^{-1}$ h^{-1}.

2. EXPERIMENTAL SECTION

2.1. Preparation of the BNs Solution. 100 mg of boron powder and 2.5 g of melamine were taken into an agate ball mill jar and ground for 24 h. Subsequently, the obtained mixture was dispersed into 260 mL of solution (isopropanol to water ratio of 1:1) to form a mixed solution at a mass concentration of 10 mg mL^{-1}. Finally, ultrasonic exfoliation for 5 h (200 W) and centrifugation at a speed of 3000 rpm for 30 min were performed to obtain the supernatant, which is the BNs solution.

2.2. Synthesis of the f-B_s-C, f-B_p-C, f-Pure C, and B_s-C. First, 250 mg of partially oxidized activated carbon was added to 40 mL of BNs solution, and then, it was subjected to ultrasonication for 4 h to disperse it evenly. Next, the mixture was vigorously stirred and heated on a hot plate to 100 °C, allowing the mixture to evaporate to dryness to obtain the precursor. Finally, the resulting precursor was treated in an FJH device under an Ar atmosphere (50 sccm) and heated up to 3000 °C within 1 s and maintained for 30 s to obtain the f-B_s-C (also known as f-B_s-C-40) catalyst. f-B_s-C-20 and f-B_s-C-60 were synthesized by adding 20 and 60 mL of the BNs solution, respectively, and the other conditions were the same as those for f-B_s-C. The oxidized activated carbon was synthesized based on reported studies by replacing only multiwalled carbon nanotubes with coconut shell−activated carbon.[28]

f-B_p-C and f-pure C were synthesized using the same heating conditions as those for the f-B_s-C, and the only difference was that the BNs filtrate was obtained by first filtering the BNs solution with a filter membrane of 0.22 μm. Subsequently, only 15 mg of boron powder and 385 mg of melamine were added to 40 mL of BNs filtrate to obtain the precursors for the preparation of f-B_p-C and f-pure C, respectively.

B_s-C was synthesized using the same precursor as that for f-B_s-C, except for the use of a traditional quartz tube furnace heating device. The heating conditions involved heating at a rate of 5 °C min^{-1} under an Ar atmosphere (20 sccm), reaching 1100 °C and maintaining it for 1 h.

3. RESULTS AND DISCUSSION

3.1. Morphological Characterization. Boron powder was first exfoliated into nanosheets to reduce the size of the B precursor. The oxidized coconut shell−activated carbon was uniformly dispersed in BNs solution by ultrasonic treatment. Subsequently, the dried mixture was flash heated under an Ar atmosphere at a temperature of 3000 °C for 30 s, as shown in Figure 1. During this process, the BNs were partially

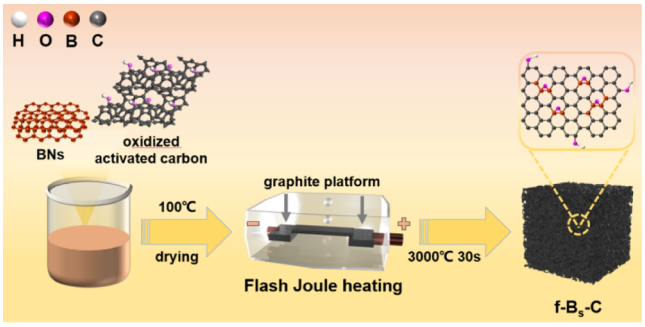

Figure 1. Schematic illustration of the synthesis of f-B_s-C.

decomposed and simultaneously doped into the carbon matrix (f-B_s-C) by forming B−C bonds.[27,29] A general pyrolysis progress (1100 °C for 1 h) was applied to prepare the control sample (B_s-C) using a quartz tube furnace, and the other conditions were the same as those for f-B_s-C. We also fabricated the other two control samples by the FJH process, boron powder doped carbon (f-B_p-C) and pure carbon (f-pure C).

In high-resolution transmission electron microscopy (HR-TEM) and atomic force microscopy (AFM) images of BNs, the BNs obtained by liquid exfoliation showed a multiple layer nanosheet structure with a thickness of over 20 nm (Figures S1 and S2).[6,30] The lattice fringe spacings were 0.243, 0.301, 0.332, and 0.342 nm, as shown in Figure S1, corresponding to the (215), (302), (104), and (203) planes of BNs (Figure S3). In the scanning electron microscopy (SEM) and HR-TEM images, f-B_s-C showed a three-dimensional bulk structure (Figures S4 and 2a), and in the enlarged HR-TEM image (Figure 2b), abundant fringe areas with a clear spot lattice of the (002) plane in the fast Fourier transform (FFT) pattern and the layer spacing of 0.361 nm corresponding to the (002) plane of graphene were observed.[31,32] On the contrary, f-pure C showed a dizzy FFT pattern with a (002) layer spacing of 0.342 nm (Figures 2c and S5). Compared to f-pure C, the larger layer spacing in f-B_s-C can be attributed to the B atom doping by decomposing BNs.[33,34] In the case of f-B_p-C, numerous distinct B nanoparticles were dispersed throughout the carbon matrix. This dispersion was attributed to the use of large-sized B powder, which was not fully decomposed during the Joule heating process, as shown in Figure S6. As predicted, the B_s-C showed the amorphous structure in the HR-TEM image because of the low graphitization degree at a low pyrolysis temperature (Figure S7). The high-angle annular dark-field scanning transmission electron microscopy (HAADF-STEM) image and element mapping images (Figure 2d) showed uniform mappings of C, B, and O elements, which demonstrated the uniform distribution of B dopants in f-B_s-C.

f-B_s-C, f-B_p-C, and f-pure C exhibited narrow and high-intensity (002) characteristic peaks of the carbon material, indicating a highly crystalline structure in X-ray diffraction

https://doi.org/10.1021/acsanm.4c02704
ACS Appl. Nano Mater. 2024, 7, 18912−18919

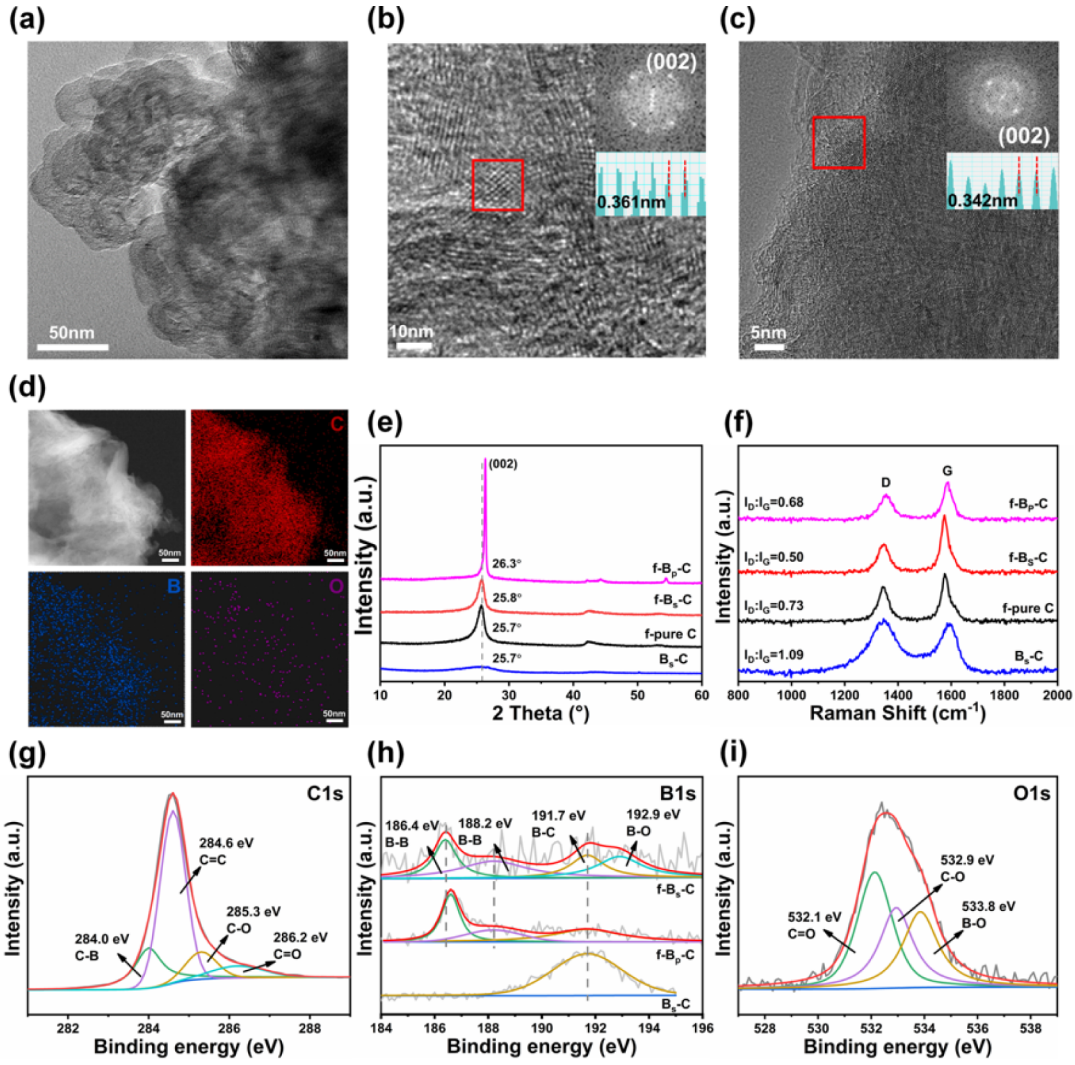

Figure 2. (a,b) HR-TEM images of f-B$_s$-C. (c) HR-TEM image of f-pure C. (d) HAADF-STEM image of f-B$_s$-C and the corresponding energy-dispersive X-ray spectroscopy elemental mapping images of C, B, and O. (e) XRD patterns of f-B$_s$-C, f-B$_p$-C, f-pure C, and B$_s$-C. (f) Raman spectra of f-B$_s$-C, f-B$_p$-C, f-pure C, and B$_s$-C. (g) High-resolution XPS spectra of C 1s in f-B$_s$-C. (h) High-resolution XPS spectra of B 1s in f-B$_s$-C, f-B$_p$-C, and B$_s$-C. (i) High-resolution XPS spectra of O 1s in f-B$_s$-C.

(XRD) images (Figure 2e). Compared to B$_s$-C, the samples prepared by the FJH method showed an increasing (002) peak intensity, demonstrating higher graphitization degree.[35] In the Raman spectra (Figure 2f), all samples exhibited two prominent bands corresponding to the D band (sp^3 amorphous carbon) and the G band (graphitic microcrystalline structure). The ratio value of I_D/I_G (intensity ratio of D band to G band) is used to represent the defect degree by sp^3 to sp^2 hybridized carbon.[36,37] Compared to B$_s$-C (1.09), f-B$_p$-C (0.68), and f-pure C (0.73), the I_D/I_G ratio of f-B$_s$-C (0.50) was greatly smaller, indicating a higher degree of graphitization; this also proves that the transient ultrahigh temperature process is beneficial in improving the graphite degree of carbon material.[38] Meanwhile, the two-dimensional sheet structure of BNs properly promoted the graphitization of carbon material by acting as a substrate in f-B$_s$-C.[39,40]

Through X-ray photoelectron spectroscopy (XPS), we further investigated the chemical composition and heteroatom configuration, and the elemental contents of all samples are summarized in Table S1. In Figure 2g, the high-resolution C 1s spectrum of f-B$_s$-C exhibits four fitting peaks at 284.0 284.6, 285.3, and 286.2 eV, corresponding to B−C, C═C, C−O, and C═O bonds, respectively. The B−C peak in f-B$_s$-C demonstrated a covalent bond formation between B dopants and the carbon matrix. In the high-resolution B 1s spectrum of f-B$_s$-C (Figure 2h), there were four fitting peaks: peaks at 191.7 and 192.9 eV assigned to B−C and B−O bonds, respectively,[28] while the peaks at 186.4 and 188.2 eV originated from B−B bonds,[41,42] indicating the incorporation of B−B covalent bonds in the biomass carbon material. For f-B$_p$-C, there were stronger B−B peak intensities due to the large size boron powder (Figures 2h and S8). As shown in Figures 2h and S9, compared to f-B$_s$-C, B$_s$-C lacked the characteristic peaks of B−B bonds; this difference can be attributed to the variations in pyrolysis conditions. Under long pyrolysis time (1100 °C for 1 h), the BNs were completely decomposed into single B atoms in B$_s$-C. Due to the usage of melamine during the preparation of BNs solution, many N atoms were doped into catalysts, as summarized in Table S1. The N configurations can be fitted into pyridinic-N, pyrrolic-N, and graphitic-N, as shown in Figure S10.[43] Furthermore, the O 1s spectrum of f-B$_s$-C is characterized by using three distinct peaks: 532.1 eV (C═O),

https://doi.org/10.1021/acsanm.4c02704
ACS Appl. Nano Mater. 2024, 7, 18912−18919

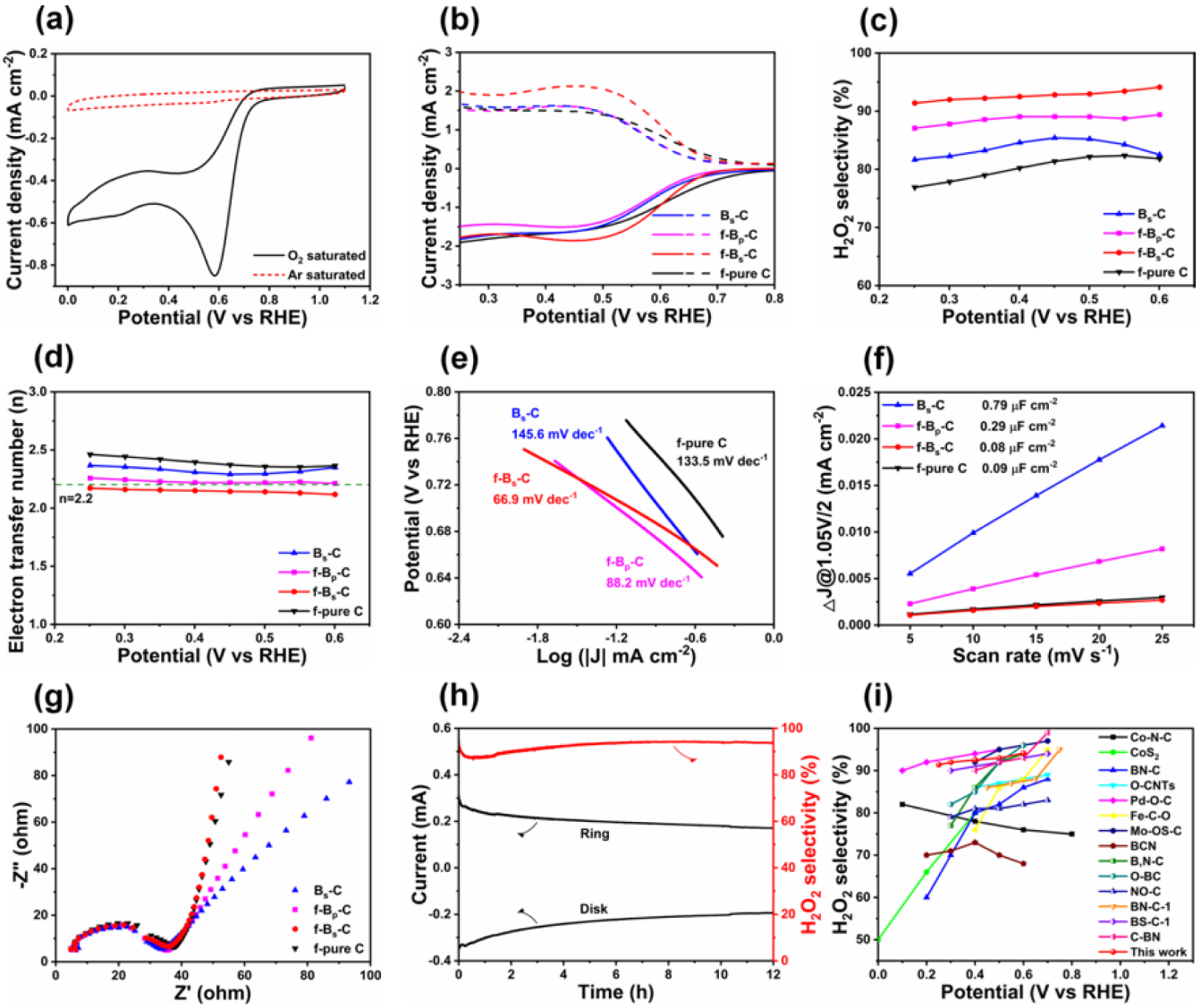

Figure 3. (a) CV measurements of f-B_s-C for ORR in Ar-saturated and O_2-saturated electrolytes, respectively. (b) LSV measurements of f-B_s-C, f-B_p-C, f-pure C, and B_s-C. (c,d) The corresponding H_2O_2 selectivity and electron transfer numbers were calculated from the LSV curves of f-B_s-C, f-B_p-C, f-pure C, and B_s-C. (e) The curves of the Tafel value for f-B_s-C, f-B_p-C, f-pure C, and B_s-C. (f) The ECSAs of f-B_s-C, f-B_p-C, f-pure C, and B_s-C were calculated from CV curves at different scan rates. (g) EIS spectra for f-B_s-C, f-B_p-C, f-pure C, and B_s-C. (h) Long-term stability measurement of f-B_s-C. (i) Comparison of H_2O_2 selectivity to many recently reported electrocatalysts.

532.9 eV (C−O), and 533.8 eV (B−O) (Figure 2i).[32] According to the HR-TEM characterization and XPS analysis, we speculated that the BNs can partially decompose into multiple B−B bonds and be doped into the biomass carbon matrix under the FJH treatment process.

3.2. Electrocatalytic Performance for H_2O_2 Generation. To verify the capability of different catalysts in the $2e^-$ ORR, we employed a standard three-electrode RRDE setup for testing the catalytic activity and selectivity in an alkaline environment (0.1 M KOH). Prior to the tests, high-purity O_2 was bubbled into the electrolyte for 20 min. During electrochemical testing, the electrolyte was placed in a dark state to minimize the degradation of low-concentration H_2O_2 as much as possible. We maintained the ring electrode at 1.2 V vs RHE to oxidize the H_2O_2 produced by the disk electrode, while simultaneously keeping the RRDE electrode rotation speed at 1600 rpm.[22] The collection efficiency of H_2O_2 was calibrated to be 0.37. As shown in Figure 3a, f-B_s-C exhibited a CV curve without any noticeable peak in the Ar-saturated solution, while a well-defined redox peak in the O_2 saturated electrolyte, indicating f-B_s-C with significant electrocatalytic activity for oxygen reduction.[44] As shown in Figure 3b, all catalysts show current density curves, where solid and dashed lines represent the current generated by the reduction of O_2 at the disk and partially oxidized H_2O_2 at the Pt ring, respectively. Meanwhile, in comparison to f-B_p-C, f-pure C, and B_s-C, f-B_s-C showed the highest ring current density, suggesting its preferable activity to $2e^-$ ORR. In Figure 3c,d, f-B_s-C had the highest H_2O_2 selectivity of 91−94% in the potential range of 0.25−0.6 V vs RHE. The calculated electron transfer number was lower than 2.2, further demonstrating the great $2e^-$ ORR performance of f-B_s-C.[45] In contrast, the control samples of f-B_p-C, f-pure C, and B_s-C reached only 87−89%, 76−81%, and 81−82%, respectively. In addition, the ratio of B dopant/biomass carbon in the catalyst was also optimized by adding different contents of BNs solution, and the correspond-

https://doi.org/10.1021/acsanm.4c02704
ACS Appl. Nano Mater. 2024, 7, 18912−18919

ing catalysts were defined with f-B_s-C-x (BNs solution volume, x = 20, 40, 60 mL). The results showed that the optimal catalyst was f-B_s-C-40 (f-B_s-C) (Figure S11). Notably, although B_s-C contained an abundance of oxygen functional groups, it exhibited the lowest H_2O_2 selectivity, which suggested that the high H_2O_2 selectivity observed in f-B_s-C is not due to the presence of oxygen functional groups.[46] Compared to f-B_s-C, B_s-C lacking B−B covalent bonds exhibited significantly lower catalytic activity and selectivity, emphasizing the crucial role of B−B covalent bond dopants in the 2e$^-$ ORR performance.[23] f-B_p-C prepared by using large-sized boron powder as a B atom dopant contains characteristic B−B bond peaks with a higher intensity than that of f-B_s-C, but f-B_p-C still shows slightly lower selectivity than that of f-B_s-C, indicating the great effect of the B precursor on the catalytic capability.

Moreover, through the kinetic comparison of the four catalysts (Figure 3e), the Tafel value of f-B_s-C (66.9 mV dec^{-1}) was much lower than that of f-B_p-C (88.2 mV dec^{-1}), f-pure C (133.5 mV dec^{-1}), and B_s-C (145.6 mV dec^{-1}), indicating that f-B_s-C exhibits greatly more rapid kinetics to the 2e$^-$ ORR.[47] The low Tafel value may be due to the abundance of activity sites present in f-B_s-C, as demonstrated in the following density functional theory simulation. Figures 3f and S12 show that, compared to f-B_p-C, f-pure C, and B_s-C, f-B_s-C had the lowest electrochemical active surface area (ECSA), suggesting a lower active site density.[48,49] The low ECSA can be attributed to the low specific surface area (SSA) in f-B_s-C (Figure S13). Therefore, the excellent electrocatalytic capability of f-B_s-C is derived from the inherent activity of the B atom dopants. From the electrochemical impedance spectroscopy (EIS) plot shown in Figure 3g, among all samples, f-B_s-C had the smallest semicircle (left side) and the steepest slope of the curve (right side), representing lower charge transfer resistance and faster mass transfer velocity.[50] Furthermore, we evaluated the stability of f-B_s-C through a prolonged current−time curve test (Figure 3h). After continuous operation at a fixed disk potential of 0.5 V vs RHE for 12 h, the H_2O_2 selectivity of f-B_s-C remained over 90%, demonstrating outstanding electrochemical stability. Meanwhile, the H_2O_2 selectivity of f-B_s-C was at a high level compared to many recently reported electrocatalysts (Figure 3i and Table S2).

To further assess the ability of f-B_s-C in practical electrocatalytic 2e$^-$ ORR production of H_2O_2, we assembled an actual three-electrode flow cell setup (Figures 4a and S14) under high current density conditions.[1] The setup employed a Pt film as the anode, a gas diffusion layer (GDL) electrode coated with the f-B_s-C (1 mg cm^{-2}) as the cathode, and an Ag/AgCl as the reference electrode.[48] As shown in Figure 4b, in the LSV curve, the current density rapidly reached 147 mA cm^{-2} at a low potential of −1.2 V vs RHE. Subsequently, at a fixed potential (potential at a current density of ∼50 mA cm^{-2}) of 0.1 V vs RHE, the stability of f-B_s-C was tested using a long-time i−t curve. After 11 h of testing, it can be noticed that the current density remained nearly unchanged (Figure 4c). Using Ce^{4+} titration to detect H_2O_2 in the electrolyte (Figures 4d and S15), the H_2O_2 concentration was increased to 19.4 mM (total H_2O_2 production of 183 mg) during 11 h of testing, further demonstrating the excellent stability of f-B_s-C. Within the initial 1 h, the H_2O_2 production rate reached 798 mmol $g_{catalyst}^{-1}$ h^{-1}, which exceeded that of the majority of catalysts (see detail in Table S3). The Faradaic efficiency (FE%) of H_2O_2 surpassed 90% in the first 6 h, maintaining above 80%

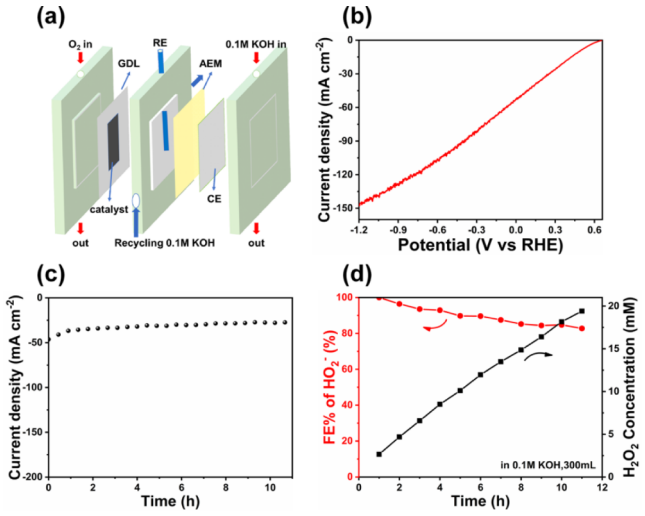

Figure 4. (a) Schematic illustration of the actual flow cell setup. (b) The LSV curve of f-B_s-C. (c) The i−t curve for H_2O_2 production at a fixed potential of 0.1 V vs RHE during 11 h of testing. (d) FE% of H_2O_2 (left) and H_2O_2 produced concentration (right) during 11 h measurement.

until 11 h. The preserved high FE% surpasses most electrocatalysts measured by flow cell setups.[51]

3.3. DFT Simulation. Density functional theory (DFT) calculations were performed to understand the high selectivity of H_2O_2. The internal carbon skeleton structures of f-B_s-C (Figure 5a−f) were analyzed based on the XPS analysis,

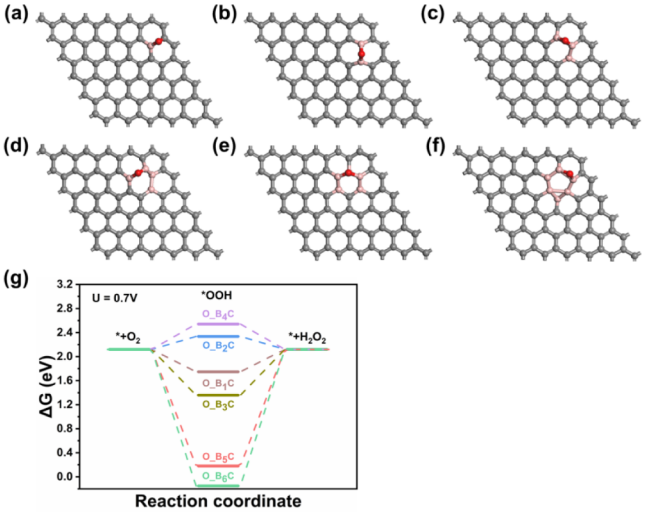

Figure 5. Optimized models of (a) O−B_1−C, (b) O−B_2−C, (c) O−B_3−C, (d) O−B_4−C, (e) O−B_5−C, and (f) O−B_6-C; (g) ΔG of the 2e$^-$ ORR reaction pathway for optimization models of O−B_1−C, O−B_2−C, O−B_3−C, O−B_4−C, O−B_5−C, and O−B_6−C.

particularly focusing on different numbers of B−B bonds in the carbon matrix. Generally, when the 2e$^-$ ORR tends infinitely to thermodynamic equilibrium, the potential of each intermediate state of its reaction process remains at an actual potential of 0.7 V vs RHE.[52] O−B_2−C exhibited the lowest overpotential (0.21 eV) for H_2O_2 production, as shown in Figure 5g, suggesting its preferable reactivity in generating H_2O_2. This characteristic of O−B_2−C highlighted its potential as an efficient catalyst in reactions where H_2O_2 formation was desired. For the other

https://doi.org/10.1021/acsanm.4c02704
ACS Appl. Nano Mater. 2024, 7, 18912−18919

models, the Gibbs free energy (ΔG) of pure C, O−B_1−C, O−B_3−C, O−B_4−C, O−B_5−C, and O−B_6−C were 0.79, 0.37, 0.76, 0.42, 1.94, and 2.27 eV (Figures 5g and S16), respectively, and the corresponding order of reaction rate was O−B_2−C > O−B_1−C > O−B_4−C > pure C > O−B_3−C > O−B_5−C > O−B_6−C. Meanwhile, the pyridinic-N, pyrrolic-N, and graphitic-N formed in the N-doped carbon materials (N−C) were simulated (Figure S16) and their ΔG was lower than that of the optimal model O−B_2−C.[53,54] Compared to f-B_s-C, the other catalysts showed much higher N contents but with lower catalytic performance (Table S1), indicating that the doped N atoms were not the main catalytic active sites, as demonstrated by DFT simulation of N configurations. The calculated results indicated that oxidized B−B bonds can promote $2e^-$ ORR, which was consistent with the characterization and electrochemical data. However, with the increase in B−B bonds, the catalytic performance decreased, which can be attributed to the interference of excess B−B bonds in the formation of active catalytic sites, reducing the interaction capability with reactants. Moreover, too many B−B bonds can lead to structural instability in the catalyst, thereby diminishing the number of effective catalytic sites. Thus, controlling the quantity of B−B bonds is crucial for enhancing the catalytic performance.

4. CONCLUSION

In summary, we successfully doped B atoms into a biomass carbon nanomaterial by the FJH method. The HR-TEM and XPS characterization demonstrated that the crystal structure of BNs was partially decomposed, and the B−B bonds remained in the carbon matrix. The electrocatalysis measurement with RRDE and flow cell demonstrated the preferable $2e^-$ ORR performance including high H_2O_2 selectivity, stability, and mass activity. The DFT simulation revealed that O atoms on B−B effectively enhanced the catalytic activity of active sites.

■ ASSOCIATED CONTENT

Supporting Information

The Supporting Information is available free of charge at https://pubs.acs.org/doi/10.1021/acsanm.4c02704.

Experimental details; TEM, XRD, AFM, SEM, XPS, BET, electrochemical test data; photographs of the experimental setup; the elemental content of all samples; and comparison of the catalytic performance (PDF)

■ AUTHOR INFORMATION

Corresponding Authors

Shengchun Hu − *Key Lab of Biomass Energy and Material, Jiangsu Province, Jiangsu Co-Innovation Center of Efficient Processing and Utilization of Forest Resources, Institute of Chemical Industry of Forest Products, Chinese Academy of Forestry, Nanjing 210042, China*; Email: hushengchun@icifp.cn

Mengmeng Fan − *Jiangsu Co-Innovation Center of Efficient Processing and Utilization of Forest Resources, International Innovation Center for Forest Chemicals and Materials, College of Chemical Engineering, Nanjing Forestry University, Nanjing 210037, China; Key Lab of Biomass Energy and Material, Jiangsu Province, Jiangsu Co-Innovation Center of Efficient Processing and Utilization of Forest Resources, Institute of Chemical Industry of Forest Products, Chinese Academy of Forestry, Nanjing 210042, China*; orcid.org/0000-0002-4226-9142; Email: fanmengmeng370@njfu.edu.cn

Authors

Xiang Xu − *Jiangsu Co-Innovation Center of Efficient Processing and Utilization of Forest Resources, International Innovation Center for Forest Chemicals and Materials, College of Chemical Engineering, Nanjing Forestry University, Nanjing 210037, China*

Ruting Xu − *Key Lab of Biomass Energy and Material, Jiangsu Province, Jiangsu Co-Innovation Center of Efficient Processing and Utilization of Forest Resources, Institute of Chemical Industry of Forest Products, Chinese Academy of Forestry, Nanjing 210042, China*

Yuying Zhao − *Key Lab of Biomass Energy and Material, Jiangsu Province, Jiangsu Co-Innovation Center of Efficient Processing and Utilization of Forest Resources, Institute of Chemical Industry of Forest Products, Chinese Academy of Forestry, Nanjing 210042, China; School of Chemical Sciences, The University of Auckland, Auckland 1010, New Zealand*

Yuhan Wu − *Jiangsu Co-Innovation Center of Efficient Processing and Utilization of Forest Resources, International Innovation Center for Forest Chemicals and Materials, College of Chemical Engineering, Nanjing Forestry University, Nanjing 210037, China*

Qixin Yuan − *Jiangsu Co-Innovation Center of Efficient Processing and Utilization of Forest Resources, International Innovation Center for Forest Chemicals and Materials, College of Chemical Engineering, Nanjing Forestry University, Nanjing 210037, China*

Kang Sun − *Key Lab of Biomass Energy and Material, Jiangsu Province, Jiangsu Co-Innovation Center of Efficient Processing and Utilization of Forest Resources, Institute of Chemical Industry of Forest Products, Chinese Academy of Forestry, Nanjing 210042, China*

Jianchun Jiang − *Jiangsu Co-Innovation Center of Efficient Processing and Utilization of Forest Resources, International Innovation Center for Forest Chemicals and Materials, College of Chemical Engineering, Nanjing Forestry University, Nanjing 210037, China; Key Lab of Biomass Energy and Material, Jiangsu Province, Jiangsu Co-Innovation Center of Efficient Processing and Utilization of Forest Resources, Institute of Chemical Industry of Forest Products, Chinese Academy of Forestry, Nanjing 210042, China*

Complete contact information is available at: https://pubs.acs.org/10.1021/acsanm.4c02704

Notes

The authors declare no competing financial interest.

■ ACKNOWLEDGMENTS

This work was supported by the Key Laboratory of Biomass Energy and Material, Jiangsu Province (JSBEM-S-202315), the National Natural Science Foundation of China (no. 32371810), the Foundation Research Project of Jiangsu Province (BK20221338), the China Postdoctoral Science Foundation (no. 2023M731702), the Jiangsu Co-Innovation Center of Efficient Processing and Utilization of Forest Resources, the International Innovation Center for Forest Chemicals and Materials, Nanjing Forestry University, and the merit-based funding for Nanjing innovation and technology project.

REFERENCES

(1) Tian, Y.; Deng, D.; Xu, L.; Li, M.; Chen, H.; Wu, Z.; Zhang, S. Strategies for Sustainable Production of Hydrogen Peroxide via Oxygen Reduction Reaction: From Catalyst Design to Device Setup. *Nano-Micro Lett.* **2023**, *15*, 122.

(2) Liu, K.; Chen, P.; Sun, Z.; Chen, W.; Zhou, Q.; Gao, X. The atomic interface effect of single atom catalysts for electrochemical hydrogen peroxide production. *Nano Res.* **2023**, *16*, 10724−10741.

(3) Peng, W.; Tan, H.; Liu, X.; Hou, F.; Liang, J. Perspectives on Carbon-Based Catalysts for the Two-Electron Oxygen Reduction Reaction for Electrochemical Synthesis of Hydrogen Peroxide: A Minireview. *Energy Fuels* **2023**, *37*, 17863−17874.

(4) Guo, Y.; Tong, X.; Yang, N. Photocatalytic and Electrocatalytic Generation of Hydrogen Peroxide: Principles, Catalyst Design and Performance. *Nano-Micro Lett.* **2023**, *15*, 77.

(5) Song, M.; Liu, W.; Zhang, J.; Zhang, C.; Huang, X.; Wang, D. Single-Atom Catalysts for H_2O_2 Electrosynthesis via Two-Electron Oxygen Reduction Reaction. *Adv. Funct. Mater.* **2023**, *33*, 2212087.

(6) Li, L.; Tang, C.; Zheng, Y.; Xia, B.; Zhou, X.; Xu, H.; Qiao, S. Z. Tailoring Selectivity of Electrochemical Hydrogen Peroxide Generation by Tunable Pyrrolic-Nitrogen-Carbon. *Adv. Energy Mater.* **2020**, *10*, 2000789.

(7) Ren, X.; Dong, X.; Liu, L.; Hao, J.; Zhu, H.; Liu, A.; Wu, G. Research progress of electrocatalysts for the preparation of H_2O_2 by electrocatalytic oxygen reduction reaction. *SusMat* **2023**, *3*, 442−470.

(8) Zhao, D.; Zhuang, Z.; Cao, X.; Zhang, C.; Peng, Q.; Chen, C.; Li, Y. Atomic site electrocatalysts for water splitting, oxygen reduction and selective oxidation. *Chem. Soc. Rev.* **2020**, *49*, 2215−2264.

(9) Lim, J. S.; Kim, J. H.; Woo, J.; Baek, D. S.; Ihm, K.; Shin, T. J.; Sa, Y. J.; Joo, S. H. Designing highly active nanoporous carbon H_2O_2 production electrocatalysts through active site identification. *Chem* **2021**, *7*, 3114−3130.

(10) Xu, X.; Zhao, Y.; Yuan, Q.; Wu, Y.; He, J.; Fan, M. Porous heterostructure of h-BN/carbon as an efficient electrocatalyst for hydrogen peroxide generation. *Carbon Lett.* **2024**, *34*, 1629−1637.

(11) Zhang, D.; Mitchell, E.; Lu, X.; Chu, D.; Shang, L.; Zhang, T.; Amal, R.; Han, Z. Metal-free carbon-based catalysts design for oxygen reduction reaction towards hydrogen peroxide: From 3D to 0D. *Mater. Today* **2023**, *63*, 339−359.

(12) Zhao, Y.; Raj, J.; Xu, X.; Jiang, J.; Wu, J.; Fan, M. Carbon Catalysts Empowering Sustainable Chemical Synthesis via Electrochemical CO_2 Conversion and Two-Electron Oxygen Reduction Reaction. *Small* **2024**, 2311163.

(13) Wang, S.; Ye, D.; Liu, H.; Zhu, X.; Liu, Z.; Chen, R.; Liao, Q.; Yang, Y. Natural bamboo-derived O-doped rocky electrocatalyst for high-efficiency electrochemical reduction of O_2 to H_2O_2. *Int. J. Hydrogen Energy* **2022**, *47*, 5961−5973.

(14) Gao, Z.; Zhu, Q.; Cao, Y.; Wang, C.; Liu, L.; Zhu, J. Design strategies of carbon-based single-atom catalysts for efficient electrochemical hydrogen peroxide production. *J. Environ. Chem. Eng.* **2023**, *11*, 109572.

(15) Byeon, A.; Yun, W. C.; Kim, J. M.; Lee, J. W. Recent progress in heteroatom-doped carbon electrocatalysts for the two-electron oxygen reduction reaction. *Chem. Eng. J.* **2023**, *456*, 1410542.

(16) Zhang, C.; Shen, W.; Guo, K.; Xiong, M.; Zhang, J.; Lu, X. A Pentagonal Defect-Rich Metal-Free Carbon Electrocatalyst for Boosting Acidic O_2 Reduction to H_2O_2 Production. *J. Am. Chem. Soc.* **2023**, *145*, 11589−11598.

(17) Yang, Z.; Gao, Y.; Zuo, L.; Long, C.; Yang, C.; Zhang, X. Tailoring Heteroatoms in Conjugated Microporous Polymers for Boosting Oxygen Electrochemical Reduction to Hydrogen Peroxide. *ACS Catal.* **2023**, *13*, 4790−4798.

(18) Guo, Y.; Tang, C.; Cao, C.; Hu, X. N-doped carbon-based catalysts in situ generation hydrogen peroxide via 2-electron oxygen reduction reaction for degradation of organic contaminants in heterogeneous electro-Fenton process: A mini review. *Surf. Interfaces* **2023**, *38*, 102879.

(19) Liu, L.; Kang, L.; Chutia, A.; Feng, J.; Michalska, M.; Ferrer, P.; Grinter, D. C.; Held, G.; Tan, Y.; Zhao, F.; Guo, F.; Hopkinson, D. G.; Allen, C. S.; Hou, Y.; Gu, J.; Papakonstantinou, I.; Shearing, P. R.; Brett, D. J. L.; Parkin, I. P.; He, G. Spectroscopic Identification of Active Sites of Oxygen-Doped Carbon for Selective Oxygen Reduction to Hydrogen Peroxide. *Angew. Chem., Int. Ed.* **2023**, *62*, No. e202303525.

(20) Kim, Y. A.; Fujisawa, K.; Muramatsu, H.; Hayashi, T.; Endo, M.; Fujimori, T.; Kaneko, K.; Terrones, M.; Behrends, J.; Eckmann, A.; Casiraghi, C.; Novoselov, K. S.; Saito, R.; Dresselhaus, M. S. Raman Spectroscopy of Boron-Doped Single-Layer Graphene. *ACS Nano* **2012**, *6*, 6293−6300.

(21) Yu, X.; Han, P.; Wei, Z.; Huang, L.; Gu, Z.; Peng, S.; Ma, J.; Zheng, G. Boron-Doped Graphene for Electrocatalytic N_2 Reduction. *Joule* **2018**, *2*, 1610−1622.

(22) Xia, Y.; Zhao, X.; Xia, C.; Wu, Z. Y.; Zhu, P.; Kim, J. Y. T.; Bai, X.; Gao, G.; Hu, Y.; Zhong, J.; Liu, Y.; Wang, H. Highly active and selective oxygen reduction to H_2O_2 on boron-doped carbon for high production rates. *Nat. Commun.* **2021**, *12*, 4225.

(23) Ri, K.; Pak, S.; Sun, D.; Zhong, Q.; Yang, S.; Sin, S.; Wu, L.; Sun, Y.; Cao, H.; Han, C.; Xu, C.; Liu, Y.; He, H.; Li, S.; Sun, C. Boron-doped rGO electrocatalyst for high effective generation of hydrogen peroxide: Mechanism and effect of oxygen-enriched air. *Appl. Catal., B* **2024**, *343*, 123471.

(24) Han, Y.-C.; Liu, M.-L.; Sun, L.; Li, X.-C.; Yao, Y.; Zhang, C.; Ding, S.-Y.; Liao, H.-G.; Zhang, L.; Fan, F. R.; Moskovits, M.; Tian, Z.-Q. A general strategy for overcoming the trade-off between ultrasmall size and high loading of MOF-derived metal nanoparticles by millisecond pyrolysis. *Nano Energy* **2022**, *97*, 107125.

(25) Fogg, J. L.; Putman, K. J.; Zhang, T.; Lei, Y.; Terrones, M.; Harris, P. J. F.; Marks, N. A.; Suarez-Martinez, I. Catalysis-free transformation of non-graphitising carbons into highly crystalline graphite. *Commun. Mater.* **2020**, *1*, 47.

(26) Cheng, L.; Yeung, C. S.; Huang, L.; Ye, G.; Yan, J.; Li, W.; Yiu, C.; Chen, F.-R.; Shen, H.; Tang, B. Z.; Ren, Y.; Yu, X.; Ye, R. Flash healing of laser-induced graphene. *Nat. Commun.* **2024**, *15*, 2925.

(27) Zhao, Z.; Sun, J.; Li, Z.; Xu, X.; Zhang, Z.; Li, C.; Wang, L.; Meng, X. Rapid synthesis of efficient Mo-based electrocatalyst for the hydrogen evolution reaction in alkaline seawater with 11.28% solar-to-hydrogen efficiency. *J. Mater. Chem. A* **2023**, *11*, 10346−10359.

(28) Fan, M.; Wang, Z.; Sun, K.; Wang, A.; Zhao, Y.; Yuan, Q.; Wang, R.; Raj, J.; Wu, J.; Jiang, J.; Wang, L. N-B-OH Site-Activated Graphene Quantum Dots for Boosting Electrochemical Hydrogen Peroxide Production. *Adv. Mater.* **2023**, *35*, No. e2209086.

(29) Hou, S.; Cheng, W.; Guo, F. Fast joule-heating synthesized heteroatom-doped carbon and its impressive electrochemical performance. *Sustainable Mater. Technol.* **2023**, *35*, No. e00570.

(30) Zhang, X.; Wu, T.; Wang, H.; Zhao, R.; Chen, H.; Wang, T.; Wei, P.; Luo, Y.; Zhang, Y.; Sun, X. Boron Nanosheet: An Elemental Two-Dimensional (2D) Material for Ambient Electrocatalytic N_2-to-NH_3. *ACS Catal.* **2019**, *9*, 4609−4615.

(31) Qiu, P.; Zhu, J.; Gao, S.; Zhang, S.; Gu, J.; Liu, F.; Guo, Z. Metal-free boron catalyst with oriented crystal phase interfacial interaction for efficient electrochemical production of hydrogen peroxide. *J. Mol. Struct.* **2023**, *1291*, 135971.

(32) Fan, M.; Wang, Z.; Zhao, Y.; Yuan, Q.; Cui, J.; Raj, J.; Sun, K.; Wang, A.; Wu, J.; Sun, H.; Li, B.; Wang, L.; Jiang, J. Porous heterostructure of graphene/hexagonal boron nitride as an efficient electrocatalyst for hydrogen peroxide generation. *Carbon Energy* **2023**, *5*, No. e309.

(33) Long, Y.; Lin, J.; Ye, F.; Liu, W.; Wang, D.; Cheng, Q.; Paul, R.; Cheng, D.; Mao, B.; Yan, R. Tailoring the Atomic-Local Environment of Carbon Nanotube Tips for Selective H_2O_2 Electrosynthesis at High Current Densities. *Adv. Mater.* **2023**, *35*, No. e2303905.

(34) Chen, W.; Ge, C.; Li, J. T.; Beckham, J. L.; Yuan, Z.; Wyss, K. M.; Advincula, P. A.; Eddy, L.; Kittrell, C.; Chen, J.; Luong, D. X.; Carter, R. A.; Tour, J. M. Heteroatom-Doped Flash Graphene. *ACS Nano* **2022**, *16*, 6646−6656.

(35) Zhao, Y.; Xu, X.; Yuan, Q.; Wu, Y.; Sun, K.; Li, B.; Wang, Z.; Wang, A.; Sun, H.; Fan, M.; Jiang, J. Interfacial engineering of a vertically stacked graphene/h-BN heterostructure as an efficient

https://doi.org/10.1021/acsanm.4c02704
ACS Appl. Nano Mater. 2024, 7, 18912−18919

electrocatalyst for hydrogen peroxide synthesis. *Mater. Horiz.* **2023**, *10*, 4930−4939.
(36) Wu, D.; Yao, Z.; Sun, X.; Liu, X.; Liu, L.; Zhang, R.; Wang, C. Mussel-tailored carbon fiber/carbon nanotubes interface for elevated interfacial properties of carbon fiber/epoxy composites. *Chem. Eng. J.* **2022**, *429*, 132449.
(37) Yin, S.; Huang, Y.; Deng, C.; Jiao, Y.; Wu, W.; Seidi, F.; Xiao, H. Hierarchically porous biochar derived from orthometric integration of wooden and bacterial celluloses for high-performance electromagnetic wave absorption. *Compos. Sci. Technol.* **2022**, *218*, 109184.
(38) Kim, M.; Fernando, J. F. S.; Li, Z.; Alowasheeir, A.; Ashok, A.; Xin, R.; Martin, D.; Kumar Nanjundan, A.; Golberg, D. V.; Yamauchi, Y.; et al. Ultra-stable sodium ion storage of biomass porous carbon derived from sugarcane. *Chem. Eng. J.* **2022**, *445*, 136344.
(39) James, A. L.; Khandelwal, S.; Dutta, A.; Jasuja, K. Boron based nanosheets as reducing templates in aqueous solutions: towards novel nanohybrids with gold nanoparticles and graphene. *Nanoscale* **2018**, *10*, 20514−20518.
(40) Lu, X.; Liu, X.; Li, J.; Yao, Y.; Ma, Z.; Chang, Y.; Bao, J.; Liu, Y. Revealing the atomic-scale configuration modulation effect of boron dopant on carbon layers for H_2O_2 production. *Chem. Commun.* **2023**, *59*, 2267−2270.
(41) Wu, T.; Wu, X.; Li, L.; Hao, M.; Wu, G.; Zhang, T.; Chen, S. Anisotropic Boron-Carbon Hetero-Nanosheets for Ultrahigh Energy Density Supercapacitors. *Angew. Chem., Int. Ed.* **2020**, *59*, 23800−23809.
(42) Yu, J.; Zhou, M.; Yang, M.; Zhang, Y.; Xu, B.; Li, X.; Tao, H. Pristine and Defective 2D Borophene/Graphene Heterostructure as the Potential Anode of Lithium-Ion Batteries. *Adv. Mater. Interfaces* **2022**, *9*, 2102088.
(43) Xing, T.; Zheng, Y.; Li, L. H.; Cowie, B. C. C.; Gunzelmann, D.; Qiao, S. Z.; Huang, S.; Chen, Y. Observation of Active Sites for Oxygen Reduction Reaction on Nitrogen-Doped Multilayer Graphene. *ACS Nano* **2014**, *8*, 6856−6862.
(44) Fan, M.; Yuan, Q.; Zhao, Y.; Wang, Z.; Wang, A.; Liu, Y.; Sun, K.; Wu, J.; Wang, L.; Jiang, J. A Facile "Double-Catalysts" Approach to Directionally Fabricate Pyridinic N B-Pair-Doped Crystal Graphene Nanoribbons/Amorphous Carbon Hybrid Electrocatalysts for Efficient Oxygen Reduction Reaction. *Adv. Mater.* **2022**, *34*, 2107040.
(45) Tong, Y.; Liu, J.; Su, B. J.; Juang, J. Y.; Hou, F.; Yin, L.; Dou, S. X.; Liang, J. High-rate electrochemical H 2 O 2 production over multimetallic atom catalysts under acidic−neutral conditions. *Carbon Energy* **2024**, *6*, No. e378.
(46) Wu, Y.; Yuan, Q.; Zhao, Y.; Xu, X.; Xu, J.; Wang, Y.; Sun, K.; Wang, A.; Sun, H.; Li, B.; Xu, R.; Wang, Z.; Jiang, J.; Fan, M. Boron-Sulfur Pairs for Highly Active $2e^-$ Oxygen Reduction Reaction to Electrochemically Synthesize Hydrogen Peroxide. *ACS Sustainable Chem. Eng.* **2023**, *11*, 13363−13373.
(47) Tian, Z.; Zhang, Q.; Thomsen, L.; Gao, N.; Pan, J.; Daiyan, R.; Yun, J.; Brandt, J.; López-Salas, N.; Lai, F.; Li, Q.; Liu, T.; Amal, R.; Lu, X.; Antonietti, M. Constructing Interfacial Boron-Nitrogen Moieties in Turbostratic Carbon for Electrochemical Hydrogen Peroxide Production. *Angew. Chem., Int. Ed.* **2022**, *61*, No. e202206915.
(48) Yuan, Q.; Fan, M.; Zhao, Y.; Wu, J.; Raj, J.; Wang, Z.; Wang, A.; Sun, H.; Xu, X.; Wu, Y.; Sun, K.; Jiang, J. Facile fabrication of carbon dots containing abundant h-BN/graphite heterostructures as efficient electrocatalyst for hydrogen peroxide synthesis. *Appl. Catal., B* **2023**, *324*, 122195.
(49) Fan, M.; Xu, J.; Wang, Y.; Yuan, Q.; Zhao, Y.; Wang, Z.; Jiang, J. CO_2 Laser-Induced Graphene with an Appropriate Oxygen Species as an Efficient Electrocatalyst for Hydrogen Peroxide Synthesis. *Chem.-Eur. J.* **2022**, *28*, No. e202201996.
(50) Chang, Y.; Li, J.; Ma, J.; Liu, Y.; Xing, R.; Wang, Y.; Zhang, G. Oxygenated boron-doped carbon via polymer dehalogenation as an electrocatalyst for high-efficiency O_2 reduction to H_2O_2. *Sci. China Mater.* **2022**, *65*, 1276−1284.
(51) Chen, S.; Luo, T.; Chen, K.; Lin, Y.; Fu, J.; Liu, K.; Cai, C.; Wang, Q.; Li, H.; Li, X.; Hu, J.; Li, H.; Zhu, M.; Liu, M.; et al. Chemical Identification of Catalytically Active Sites on Oxygen-doped Carbon Nanosheet to Decipher the High Activity for Electrosynthesis Hydrogen Peroxide. *Angew. Chem., Int. Ed.* **2021**, *60*, 16607−16614.
(52) Gasteiger, H. A.; Kocha, S. S.; Sompalli, B.; Wagner, F. T. Activity benchmarks and requirements for Pt, Pt-alloy, and non-Pt oxygen reduction catalysts for PEMFCs. *Appl. Catal., B* **2005**, *56*, 9−35.
(53) Zhao, Y.; Wan, J.; Yao, H.; Zhang, L.; Lin, K.; Wang, L.; Yang, N.; Liu, D.; Song, L.; Zhu, J.; Gu, L.; Liu, L.; Zhao, H.; Li, Y.; Wang, D. Few-layer graphdiyne doped with sp-hybridized nitrogen atoms at acetylenic sites for oxygen reduction electrocatalysis. *Nat. Chem.* **2018**, *10*, 924−931.
(54) Peng, W.; Liu, J.; Liu, X.; Wang, L.; Yin, L.; Tan, H.; Hou, F.; Liang, J. Facilitating two-electron oxygen reduction with pyrrolic nitrogen sites for electrochemical hydrogen peroxide production. *Nat. Commun.* **2023**, *14*, 4430.

https://doi.org/10.1021/acsanm.4c02704
ACS Appl. Nano Mater. 2024, 7, 18912−18919